Bulk Crystalline 4H-Silicon through a Metastable Allotropic Transition

Thomas B. Shiell[1,*] Li Zhu[1], Brenton A. Cook,[2] Jodie E. Bradby,[3] Dougal G. McCulloch,[2] and Timothy A. Strobel[1,†]

[1]*Earth and Planets Laboratory, Carnegie Institution for Science, Washington, DC 20015, USA*
[2]*Physics, School of Science, RMIT University, Melbourne, Victoria 3001 Australia*
[3]*Research School of Physics, The Australian National University, Canberra, Australian Capital Territory, 2601 Australia*

We report the synthesis of bulk, highly oriented, crystalline 4H hexagonal silicon (4H-Si), through a metastable phase transformation upon heating the single-crystalline Si_{24} allotrope. Remarkably, the resulting 4H-Si crystallites exhibit an orientation relationship with the Si_{24} crystals, indicating a structural relationship between the two phases. Optical absorption measurements reveal that 4H-Si exhibits an indirect band gap near 1.2 eV, in agreement with first principles calculations. The metastable crystalline transition pathway provides a novel route to access bulk crystalline 4H-Si in contrast to previous transformation paths that yield only nanocrystalline-disordered materials.

Diamond-cubic (DC) Si is the thermodynamically stable form at ambient conditions, and represents the major constituent of electrical devices in the semiconductor industry. Over the last 50 years, several new allotropes of Si have been synthesized using a range of techniques including deposition [1], implantation [2], high pressure methodologies [3], and confined microexplosions [4]. Each of these allotropes possess unique electronic structures and physical properties, which may be advantageous to future devices and help overcome intrinsic limitations of the DC-Si structure. Among the known Si allotropes, the R8 [5], BC8 [6,7], lonsdaleite [8], and clathrate or clathratelike [9–15] structures have been stabilized and characterized at ambient conditions using bulk methods.

Hexagonal Si with various stacking schemes has been of interest since the 1960s. Theoretical calculations consistently indicate that various hexagonal allotropes possess indirect band gaps of similar magnitude to DC-Si [16,17], but tunable direct gaps might be achieved through various substitution schemes, for example using Ge [18,19], or by the application of strain [20]. A thorough description of possible hexagonal polytypes and their stacking is given by Ownby *et al.* [21] 2H-Si (lonsdaleite, analogous to the wurtzite structure for a binary system) was first identified by Wentorf and Kasper after annealing BC8-Si (a phase recovered from high-pressure conditions) in air between 200–600 °C. [8]. The same 2H-Si synthesis pathway was later confirmed by Kobliska *et al.* [22] and a similar material was produced as a by-product from a reaction-bonded Si_3N_4 experiment. [23] More recently, crystalline 2H-Si (with average crystal size ~20 μm) was physically deposited with simultaneous UV laser ablation in the form of a thin film, and identified using electron diffraction [1]. Furthermore, several studies report the synthesis of Si nanowires with varying degrees of hexagonality referred to as non-DC polytypes, [24,25] and identify many other forms with ordered hexagonal stacking synthesized via indentation, [26] deposition [1,24,27–29], and diamond machining [30,31]. Another recently discovered complex polytype is the 9R-Si structure [24,27].

Previous reports of hexagonal Si produced from BC8-Si show broad, ambiguous diffraction patterns [32] (or none at all [8,23]), broad overlapping Raman peaks [32], and tend to coexist with disordered, amorphous Si or defective nanocrystalline regions [33]. This makes the specific hexagonal product difficult to identify. On the other hand, clear evidence for 2H-Si on the nanometer scale was obtained by depositing Si on a hexagonal GaP substrate [29]. Recently, the 2H stacking sequence [8] for the product obtained by annealing recovered BC8-Si was challenged by Pandolfi *et al.* [32], who suggested that the hexagonal phase may actually be the 4H-Si structure. While their broad powder x-ray diffraction (XRD) and Raman peaks were suggestive of nanocrystals with a hexagonal stacking sequence, the transmission electron microscopy (TEM) and selective area electron diffraction (SAED) could only be described by 4H-Si. While 2H-Si and 4H-Si are both metastable with respect to DC-Si, the 4H sequence was predicted to be ~8 meV/atom lower energy than 2H. Although large crystals of 4H-Si or 4H-C had never been synthesized, isolated, and characterized, 4H-Ge has been synthesized in both powder [34] and crystalline forms [35] from allo-Ge (a metastable open-framework Ge allotrope) annealed above 200°C, which suggests the possibility of a similar route for 4H-Si from alternative precursors. Here, we demonstrate a metastable pathway to produce crystalline 4H-Si by annealing Si_{24} crystals at moderate temperature, thus providing a novel path to isolate bulk samples with exceptional crystallinity in comparison to previous work.

Si$_{24}$ is a low-density orthorhombic Si allotrope that contains zeolitelike channels along the crystallographic *a* axis [11]. While Si$_{24}$ is metastable with respect to DC-Si by $\sim$90 meV/atom, it may persist to temperatures >400 °C upon heating for durations of $\sim$15 min [10]. Nevertheless, the high-temperature and long-term stability of Si$_{24}$ remains unclear. During annealing studies to address these questions, we observed a series of new powder diffraction lines that coexist with Si$_{24}$ after long-duration heating (days) above 200°C and fully dominate the patterns above 450°C (Supplemental Material, Fig. 1). These reflections cannot be described by DC-Si and indicate the presence of an intermediate phase that forms before relaxation to the thermodynamic ground state. To understand this intermediate phase, we studied the phase transition using synchrotron x-ray diffraction with single-crystalline Si$_{24}$. Bulk single crystals of Si$_{24}$ were recently demonstrated and the same synthetic approach was followed here [9,11] (see Supplemental Material [36] for detailed methods including Refs. [11,37–45]).

The starting Si$_{24}$ crystals are oriented along [001] due to the cleavage habit in the *ab* plane [11], and exhibit sharp single-crystal diffraction spots. Upon annealing crystals sealed under vacuum in quartz tubes in a benchtop furnace, typically near 300°C for four days, the sharp single-crystal spots from Si$_{24}$ disappear, and highly oriented multicrystalline arcs appear as shown in Fig. 1(a). The arcs show sixfold symmetry indicative of a hexagonal lattice, and display an azimuthal spread of 15.3(5)°, which reflects the misorientation of individual grains. Remarkably, the preservation of orientational order in the annealed samples indicates a structural relationship between the Si$_{24}$ [001] direction and the hexagonal axis of the product. Given the large distribution of grains, we were not able to solve the hexagonal structure using conventional single-crystal XRD, however, by averaging multiple diffraction patterns over different orientations, we were able to approximate a powder pattern. The powder pattern indexes to a primitive hexagonal lattice with $a \approx 3.84$ Å, $c \approx 12.59$ Å, which is consistent with the previous reports of 4H-Si [32]. Because of the presence of preferred orientation, the data are not suitable for Rietveld refinement, however, full-profile Le Bail refinement produces excellent agreement with the 4H-Si space group $P6_3/mmc$ with lattice parameters $a = 3.837(3)$ Å, $c = 12.586(5)$ Å [Fig. 1(b)]. The XRD pattern is not consistent with other possible hexagonal stacking sequences, and compared with previous reports of bulk 2H or 4H-Si, these samples exhibit exceptional microcrystallinity [22,32].

Raman spectra of the single-crystalline Si$_{24}$ precursor and heated product are shown in Fig. 2. Recovered samples were powdered to eliminate any possible effects of crystal orientation on scattered intensity. Samples annealed over a broad range of pressure-temperature conditions produce characteristic Raman spectra that contain two strong
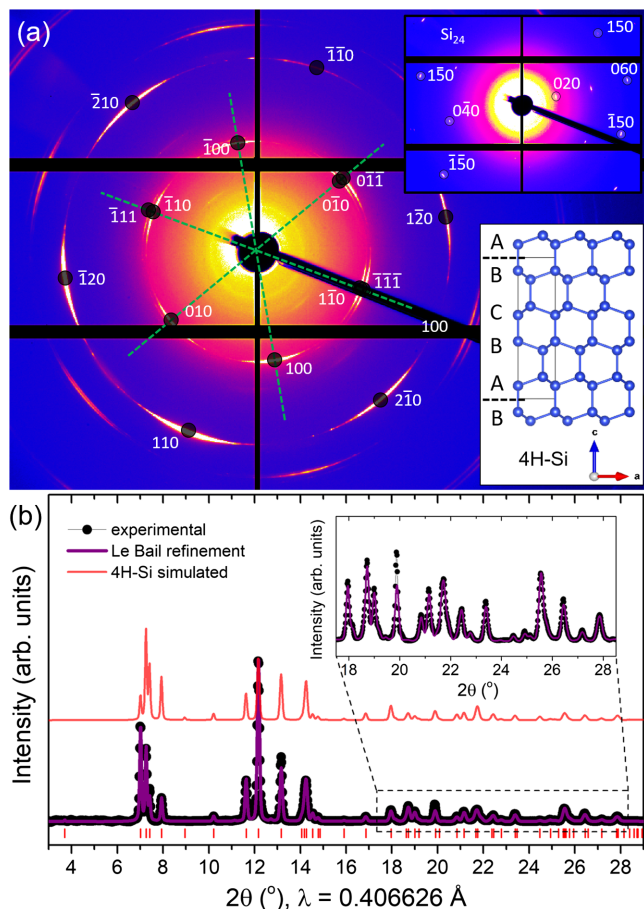

FIG. 1. (a) 2D XRD pattern of a multicrystalline 4H-Si sample produced after heating a Si$_{24}$ single crystal at 300°C for four days. The sixfold hexagonal symmetry is emphasized by green dashed lines which are at 60° intervals. Reflections in addition to those along [001] are observed as the samples were rotated with respect to the x-ray beam. The upper inset shows the single-crystalline nature of Si$_{24}$ precursor oriented along [001], and the lower inset shows a model of the 4H-Si structure with *ABCB* stacking generated using VESTA-v3 software. [46] (b) Powder diffraction pattern produced by averaging multiple sample orientations (black-dots) with Le Bail fit using GSAS-II (purple line). Allowed Bragg peaks for the 4H-Si structure are indicated by the red tick marks below the pattern. A 4H-Si powder pattern simulated using atomic positions from reference [35] is shown above the experimental data for comparison of powder averaging. A magnified high-angle region of the experimental diffraction pattern with the calculated pattern overlayed is shown in the inset.

resolvable peaks near 500 cm^{-1}, one weak peak at 416 cm^{-1}, and two very weak peaks near 100 cm^{-1}. By calculating Brillouin zone-center phonons and Raman intensities using density functional perturbation theory as implemented in Vienna *ab initio* simulation package (VASP), we generated Si Raman spectra from structures with different possible hexagonal stacking sequences (see Table 1 and Fig. 3 in Supplemental Material). The calculated Raman spectrum for 4H-Si is in excellent agreement with the experimental data with a small
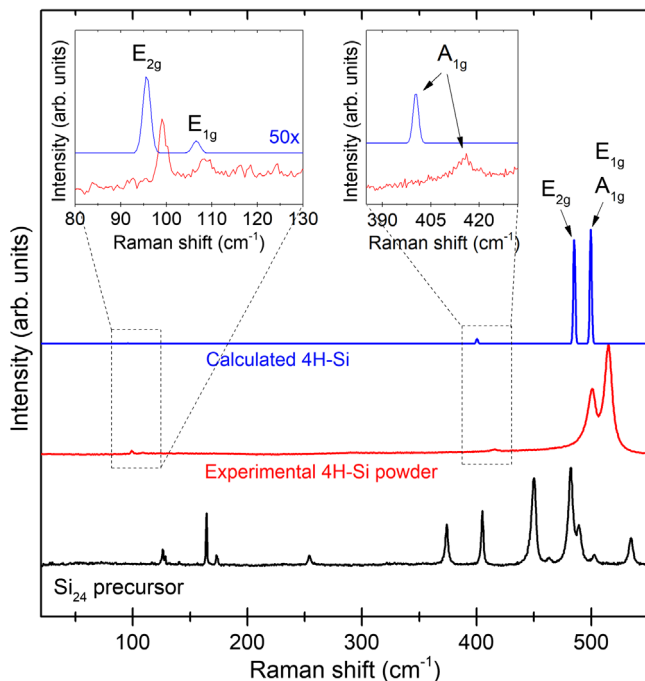
FIG. 2. Raman spectra of a Si_{24} crystal and $4H$-Si powder compared to a calculated $4H$-Si spectrum. The calculated spectrum is shown with Gaussian peaks of an arbitrary width. (inset) Regions of the Raman spectra showing that the weaker (E_{2g}, E_{1g}, and A_{1g}) peaks from the $4H$-Si calculation match the experimental observations.

consistent shift (~3%) to lower frequencies that may be explained by the static (0 K) calculation and the harmonic approximation used in the Raman calculation [47]. The calculated $4H$-Si spectrum has three intense peaks (E_{2g}, E_{1g}, and the A_{1g}) near 500 cm^{-1}, however, the calculated E_{1g} and the A_{1g} modes occur at very similar frequencies and are not resolved. This agrees with previous calculations for the hexagonal diamond polytypes of C and Si. [44,48]. The lower-frequency peaks at 100, 108, and 416 cm^{-1} are characteristic of the $4H$-Si structure and clearly distinguish this phase from other possible hexagonal stacking sequences. While the sample microstructure contributes to the width of the observed peaks, the resolution of these Raman spectra are exceptional compared with all previous bulk studies, and show all Raman-active phonon modes allowing clear disambiguation of the $4H$ hexagonal stacking sequence. Most previous spectra do not show the low-frequency modes, are broad, and/or contain significant amorphous Si [1,22,26,30,32].

To further probe the structure of the annealed material, samples were placed onto a carbon tape substrate and transferred into a focused-ion-beam (FIB, FEI Scios) for imaging and TEM sample preparation (see Supplemental Material, Fig. 4). Figures 3(a) and 3(b) show both bright and dark-field TEM images of a thinned section with crystalline grains exhibiting an average diameter of ~0.5 μm. SAED patterns of the thinned section reveals

sharp diffraction spots that index to the $\langle 100 \rangle$ zone of $4H$-Si [Fig. 3(c)]. Notably, the $\langle 100 \rangle$ zone is anticipated from FIB milling geometry, which rotates the starting [001] oriented crystals by 90° while creating the lamella. The diffraction pattern exhibits $\{00l\}$ reflections where $l = $ odd, which are formally forbidden by the $P6_3/mmc$ structure (Supplemental Material, Fig. 5). Diffraction vector analysis reveals that these reflections originate from double diffraction (dynamical scattering), which is common for DC-Si. [49] Several other measured diffraction zones obtained by tilting the sample confirm the $4H$-Si lattice with $a = 3.84(5)$ Å and $c = 12.59(7)$ Å (Supplemental Material, Fig. 6). A high-resolution TEM image of a crystalline region of the lamella is shown in Fig. 3(d). The Fourier-filtered image shown in Fig. 3(e) highlights the well-ordered layers of the $4H$-Si material with a 12.59(7) Å periodicity along the c axis, confirming the stacking sequence.

A piece of $4H$-Si (~100 μm × 100 μm × 10 μm), synthesized from a Si_{24} crystal annealed at 300°C in air, was selected for near-infrared, visible (NIR VIS) transmission measurements to probe the optical properties and electronic
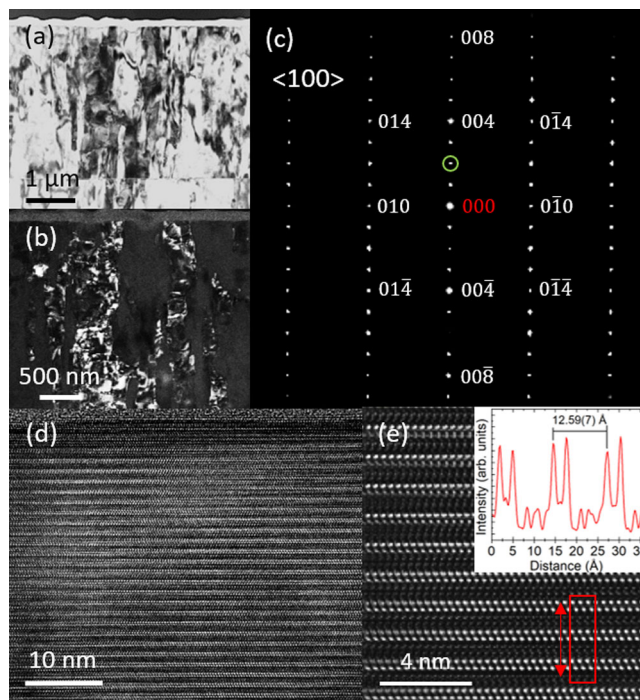

FIG. 3. (a) Bright-field TEM image of a lamella from annealed Si_{24} crystal. (b) Dark-field TEM image taken from the (002) reflection (indicated by a green circle) of the SAED pattern (c) which has been indexed to the $\langle 100 \rangle$ zone of $4H$-Si. (d) High-resolution TEM image of a $4H$-Si crystal. (e) Fourier-filtered image of a select region of (d). The inset is an intensity profile from the region inside the red rectangle which shows the 12.59(7) Å periodic spacing between layers in the $4H$-Si crystal. Note that all images and diffraction patterns are viewed along the $\langle 100 \rangle$ axis.
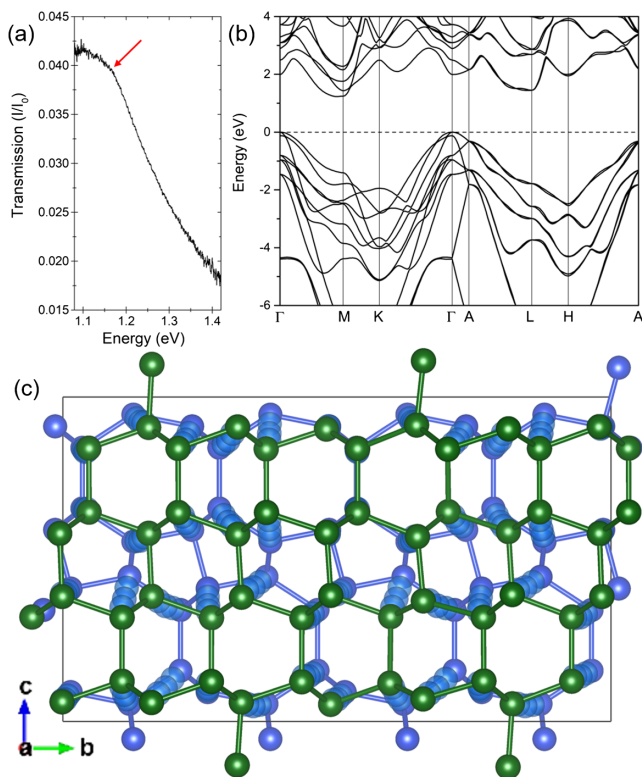
FIG. 4. (a) NIR–VIS transmission measurement of a piece of 4*H*-Si with a change in slope between 1.15–1.2 eV highlighting an absorption edge (red arrow). (b) Calculated band structure for 4*H*-Si displaying an indirect band gap ($\Gamma - M$) of 1.2 eV. (c) A ball-and-stick schematic showing the lowest-energy transition pathway from Si_{24} (blue) to 4*H*-Si (green) generated using VESTA-v3 [46]. Translucent blue spheres indicate atomic displacements during the transition.

structure. The transmission spectrum [Fig. 4(a)] shows distinct change in slope between 1.15–1.2 eV, indicating the onset of the optical band gap. The multicrystalline nature of the sample, which is composed of individual grains ~0.5 μm based on TEM, likely contributes to the width of the absorption edge. Previous calculations show indirect band gaps with similar magnitudes for Si polytypes with varying hexagonalities, and predict that the band gap of 2*H*-Si should be slightly smaller than that of DC-Si, with 4*H*-Si in between [16,17,40]. Using DFT, we estimate the band gap of 4*H*-Si using the Heyd-Scuseria-Ernzerhof (HSE06) hybrid functional, which tends to reproduce experimental values for a range of materials [45]. In agreement with previous calculations, the calculated band structure shows that 4*H*-Si is a semiconductor with an indirect band gap of ~1.2 eV ($\Gamma \rightarrow M$), matching closely with the experimental absorption results.

From a thermodynamic perspective, 4*H*-Si is metastable by 4 meV/atom (DFT PBE) with respect to DC-Si, and like the Si_{24} precursor, 4*H*-Si represents another metastable allotrope of silicon. The energetic stabilization of 4*H*-Si compared with 2*H*-Si, which is 12 meV/atom

higher than DC-Si, provides driving force to the observed stacking sequence. This energy difference also supports the claim of the 4*H*-Si (opposed to lonsdaleite) structure from the BC8 pathway [32]. We note that our energy calculations are similar to those by Raffy *et al.* using DFT LDA, which are 2.4 meV and 10.7 meV for 4*H*-Si and 2*H*-Si, respectively [17].

The crystallographic alignment of the resulting 4*H*-Si crystallites with the original Si_{24} crystals suggests an orientation relationship between the two metastable structures. To probe the underlying transition mechanism, we calculated a network of low-energy transition pathways using the Pallas method, which we recently developed to predict solid-state transition pathways [50]. Using this approach, lowest-energy pathway involves the collapse of 8-membered rings in Si_{24}, followed by the formation of intermediate states with 4-, 5-, and 7-membered rings, which ultimately transform to the 4*H* structure with exclusively 6-membered rings (Supplemental Material, Figs. 7 and 8). This lowest-energy path possesses a transition barrier of 170 meV/atom, which is significantly lower than lowest-energy transition path to DC-Si calculated to be 289 meV/atom under the same approach. While these calculations help to explain why 4*H*-Si is observed rather than DC-Si, the large unit cell (24 atoms) places limitations for adequately sampling configurational space, and lower-energy mechanisms may exist. Fortunately, the transition mechanism identified by Pallas provides significant insights into how minor atom displacements from the Si_{24} structure could lead to 4*H*-Si with retention of crystallinity. Atomic displacement vectors for the lowest-energy path from Si_{24} to 4*H*-Si are shown in Fig. 4(c). It is clear that four layers of Si atoms are present in both structures along the *c* axis, and the cell vectors are very similar. For Si_{24}, $a = 3.82$ Å, $c = 12.63$ Å [10], which is similar to 4*H*-Si in which $a = 3.84(1)$ Å, $c = 12.59(1)$ Å. Using this information, the transition path was calculated from Si_{24} to 4*H*-Si using a supercell consisting of 48 atoms using the variable cell nudged elastic band method (NEB) [51], which is suitable for larger systems, but requires the definition of atoms across the transition determined from the Pallas calculation. The NEB-optimized path determined using a 48-atom cell shows a similar mechanism to the one derived from Pallas, but the barrier is reduced to 110 meV/atom after accounting for the cell geometries (Supplemental Material, Fig. 9).

The results of this study reveal a new pathway for 4*H*-Si synthesis, which is now possible from Si_{24} and BC8-Si precursors [32]. The Si_{24} pathway appears advantageous as large crystals (>1 μm) of the parent BC8-Si phase are generally not observed. Hence, the only way to synthesize large 4*H*-Si crystals is via the Si_{24} route. Furthermore, the fact that 4*H*-Si can be formed from multiple precursors at elevated temperature (200–300°C) motivates future studies to probe the stability and transitions of other Si phases at

high temperature. The availability of large Si_{24} precursor crystals and resultant $4H$-Si product invites future studies using deposition and epitaxial growth methods, which could further enhance the quality and applications of both allotropes. The influence of strain on the optical and electrical properties of $4H$-Si is also an enticing topic for further study. Applying strain via atomic Ge substitution or via deposition growth with a mismatched lattice substrate may enhance the optical absorption properties, increase charge mobilities, or even transform $4H$-Si into a direct band gap semiconductor. Similar effects have recently been predicted for $2H$-Si using *ab initio* modeling [20].

In summary, we have shown a multistep synthesis pathway to produce crystalline $4H$-Si from a crystalline Si_{24} precursor, in contrast to previous synthesis methods which yield only disordered and amorphous materials. Optical absorption measurements reveal an indirect band gap near 1.2 eV, in close agreement with first principles calculations of the electronic band structure. If larger crystals can be synthesized and isolated, procedures could then be developed to use them as seed crystals for growing large volumes of $4H$-Si nanowires and solar devices with absorption and optoelectronic properties potentially exceeding those of DC-Si.

---

[*] tshiell@carnegiescience.edu

[†] tstrobel@carnegiescience.edu

[1] Y. Zhang, Z. Iqbal, S. Vijayalakshmi, and H. Grebel, Stable hexagonal-wurtzite silicon phase by laser ablation, Appl. Phys. Lett. **75**, 2758 (1999).

[2] A. A. Nikolskaya, D. S. Korolev, A. N. Mikhaylov, A. I. Belov, A. A. Sushkov, N. O. Krivulin, K. R. Muhamatchin, A. A. Elizarova, M. O. Marychev, A. A. Konakov, D. I. Tetelbaum, and D. A. Pavlov, Light-emitting $9R$-Si phase formed by Kr^+ ion implantation into SiO_2/Si substrate, Appl. Phys. Lett. **113**, 182103 (2018).

[3] B. Haberl, J. E. Bradby, and T. A. Strobel, Pathways to exotic metastable silicon allotropes, Appl. Phys. Rev. **3**, 040808 (2016).

[4] L. Rapp, B. Haberl, C. J. Pickard, J. E. Bradby, E. G. Gamaly, J. S. Williams, and A. V. Rode, Experimental evidence of new tetragonal polymorphs of silicon formed through ultrafast laser-induced confined microexplosion, Nat. Commun. **6**, 7555 (2015).

[5] J. M. Besson, E. H. Mokhtari, J. Gonzalez, and G. Weill, Electrical Properties of Semimetallic Silicon III and Semiconductive Silicon IV at Ambient Pressure, Phys. Rev. Lett. **59**, 473 (1987).

[6] B. D. Malone, J. D. Sau, and M. L. Cohen, *Ab initio* survey of the electronic structure of tetrahedrally bonded phases of silicon, Phys. Rev. B **78**, 035210 (2008).

[7] H. Zhang, H. Liu, K. Wei, O. O. Kurakevych, Y. Le Godec, Z. Liu, J. Martin, M. Guerrette, G. S. Nolas, and T. A. Strobel, BC8 Silicon (Si-III) is a Narrow-Gap Semiconductor, Phys. Rev. Lett. **118**, 146601 (2017).

[8] R. H. Wentorf and J. S. Kasper, Two new forms of silicon, Science **139**, 338 (1963).

[9] O. O. Kurakevych, T. A. Strobel, D. Y. Kim, T. Muramatsu, and V. V. Struzhkin, Na-Si clathrates are high-pressure phases: A melt-based route to control stoichiometry and properties, Cryst. Growth Des. **13**, 303 (2013).

[10] D. Y. Kim, S. Stefanoski, O. O. Kurakevych, and T. A. Strobel, Synthesis of an open-framework allotrope of silicon, Nat. Mater. **14**, 169 (2015).

[11] M. Guerette, M. D. Ward, L. Zhu, and T. A. Strobel, Single-crystal synthesis and properties of the open-framework allotrope Si_{24}, J. Phys. Condens. Matter **32**, 194001 (2020).

[12] J. S. Kasper, P. Hagenmuller, M. Pouchard, and C. Cros, Clathrate structure of silicon Na_8Si_{46} and Na_xSi_{136} ($X < 11$), Science **150**, 1713 (1965).

[13] Z. Jouini, O. Kurakevych, H. Moutaabbid, Y. Le Godec, M. Mezouar, and N. Guignot, Phase boundary between Na-Si clathrates of structures I and II at high pressures and high temperatures, J. Superhard Mater. **38**, 66 (2016).

[14] J. Gryko, P. F. McMillan, R. F. Marzke, G. K. Ramachandran, D. Patton, S. K. Deb, and O. F. Sankey, Low-density framework form of crystalline silicon with a wide optical band gap, Phys. Rev. B **62**, R7707(R) (2000).

[15] A. Ammar, C. Cros, M. Pouchard, N. Jaussaud, J. M. Bassat, G. Villeneuve, M. Duttine, M. Ménétrier, and E. Reny, On the clathrate form of elemental silicon, Si_{136}: Preparation and characterisation of Na_xSi_{136} ($X \rightarrow 0$), Solid State Sci. **6**, 393 (2004).

[16] C. Persson and E. Janzen, Electronic band structure in hexagonal close-packed Si polytypes, J. Phys. Condens. Matter **10**, 10549 (1998).

[17] C. Raffy, J. Furthmüller, and F. Bechstedt, Properties of hexagonal polytypes of group-IV elements from first-principles calculations, Phys. Rev. B **66**, 075201 (2002).

[18] E. A. Fitzgerald, GeSi/Si Nanostructures, Annu. Rev. Mater. Sci. **25**, 417 (1995).

[19] S. Barth, M. S. Seifner, and S. Maldonado, Metastable group IV allotropes and solid solutions: Nanoparticles and nanowires, Chem. Mater. **32**, 2703 (2020).

[20] C. Rodl, T. Sander, F. Bachstedt, J. Vidal, P. Olsson, S. Laribi, and J. F. Guillemoles, Wurtzite silicon as a potential absorber in photovoltaics: Tailoring the optical absorption by applying strain, Phys. Rev. B **92**, 045207 (2015).

[21] P. D. Ownby, X. Yang, and J. Liu, Calculated x-ray diffraction data for diamond polytypes, J. Am. Ceram. Soc. **75,** 1876 (1992).

[22] R. J. Kobliska and S. A. Solin, Raman spectrum of wurtzite silicon, Phys. Rev. B **8,** 3799 (1973).

[23] H. M. Jennings and M. H. Richman, A hexagonal (wurtzite) form of silicon, Science **193,** 1242 (1976).

[24] F. J. Lopez, U. Givan, J. G. Connell, and L. J. Lauhon, Silicon nanowire polytypes: Identification by Raman spectroscopy, generation mechanism, and misfit strain in homostructures, ACS Nano **5,** 8958 (2011).

[25] C. Cayron, M. Den Hertog, L. Latu-Romain, C. Mouchet, C. Secouard, J.-L. Rouviere, E. Rouviere, and J.-P. Simonato, Odd electron diffraction patterns in silicon nanowires and silicon thin films explained by microtwins and nanotwins, J. Appl. Crystallogr. **42,** 242 (2009).

[26] A. Kailer, Y. G. Gogotsi, and K. G. Nickel, Phase transformations of silicon caused by contact loading, J. Appl. Phys. **81,** 3057 (1997).

[27] J. L. Francisco, R. H. Eric, and L. J. Lauhon, Ordered stacking fault arrays in silicon nanowires, Nano Lett. **9,** 2774 (2009).

[28] A. Fontcuberta, I. Morral, J. Arbiol, J. D. Prades, A. Cirera, and J. R. Morante, Synthesis of silicon nanowires with wurtzite crystalline structure by using standard chemical vapor deposition, Adv. Mater. **19,** 1347 (2007).

[29] H. I. T. Hauge, M. A. Verheijen, S. Conesa-Boj, T. Etzelstorfer, M. Watzinger, D. Kriegner, I. Zardo, C. Fasolato, F. Capitani, P. Postorino, S. Kolling, A. Li, S. Assali, J. Stangl, and E. P. A. M. Bakkers, Hexagonal silicon realized, Nano Lett. **15,** 5855 (2015).

[30] B. V. Tanikella, A. H. Somasekhar, A. T. Sowers, R. J. Nemanich, and R. O. Scattergood, Phase transformations during microcutting tests on silicon, Appl. Phys. Lett. **69,** 2870 (1996).

[31] J. Yan, Laser micro-Raman spectroscopy of single-point diamond machined silicon substrates, J. Appl. Phys. **95,** 2094 (2004).

[32] S. Pandolfi, C. Renero-lecuna, Y. Le Godec, B. Baptiste, N. Menguy, M. Lazzeri, C. Gervais, K. Spektor, W. A. Crichton, and O. O. Kurakevych, Nature of hexagonal silicon forming via high-pressure synthesis: Nanostructured hexagonal 4-*H* polytype, Nano Lett. **18,** 5989 (2018).

[33] J. F. Morhange, G. Kanellis, and M. Balkanski, Raman study of laser annealed silicon, Solid State Commun. **31,** 805 (1979).

[34] E. Lopex-Cruz and M. Cardona, Raman spectra of two new modifications of germanium: Allo-germanium and 4*H*-Ge, Solid State Commun. **45,** 787 (1983).

[35] F. Kiefer, V. Hlukhyy, A. J. Karttunen, T. F. Fässler, C. Gold, E. W. Scheidt, W. Scherer, J. Nylén, and U. Häussermann, Synthesis, structure, and electronic properties of 4*H*-germanium, J. Mater. Chem. **20,** 1780 (2010).

[36] See Supplemental Material, at http://link.aps.org/supplemental/10.1103/PhysRevLett.126.215701 for more detailed methods, which includes Refs. [11,37–45].

[37] M. Guerette, M. D. Ward, K. A. Lokshin, A. T. Wong, H. Zhang, S. Stefanoski, O. Kurakevych, Y. Le Godec, S. J. Juhl, N. Alem, Y. Fei, and T. A. Strobel, Synthesis and properties of single-crystalline Na_4Si_{24}, Cryst. Growth Des. **18,** 7410 (2018).

[38] T. B. Shiell and T. A. Strobel, Compression of sodium-filled and empty open-framework Si_{24} under quasihydrostatic and nonhydrostatic conditions, Phys. Rev. B **102,** 094107 (2020).

[39] C. Prescher and V. B. Prakapenka, DIOPTAS: A program for reduction of two-dimensional x-ray diffraction data and data exploration, High Press. Res. **35,** 223 (2015).

[40] G. Kresse and J. Furthmuller, Efficient iterative schemes for ab initio total-energy calculations using a plane-wave basis set, Phys. Rev. B **54,** 11169 (1996).

[41] G. Kresse and D. Joubert, From ultrasoft pseudopotentials to the projector augmented wave method, Phys. Rev. B **59,** 1758 (1999).

[42] J. P. Perdew, K. Burke, and M. Ernzerhof, Generalized Gradient Approximation Made Simple, Phys. Rev. Lett. **77,** 3865 (1996).

[43] P. E. Blochl, Projector augmented-wave method, Phys. Rev. B **50,** 17953 (1994).

[44] A. Fonari and S. Stauffer, VASP_Raman. Py., https://Github.Com/Raman-Sc/VASP/ (2013).

[45] J. Heyd, G. E. Scuseria, and M. Ernzerhof, Hybrid functionals based on a screened Coulomb potential, J. Chem. Phys. **118,** 8207 (2003).

[46] K. Momma and F. Izumi, VESTA3 for three-dimensional visualization of crystal, volumetric and morphology data, J. Appl. Crystallogr. **44,** 1272 (2011).

[47] D. Porezag and M. R. Pederson, Infrared intensities and Raman-scattering activities within density-functional-theory, Phys. Rev. B **54,** 7830 (1996).

[48] K. E. Spear, A. W. Phelps, and W. B. White, Diamond polytypes and their vibrational-spectra, J. Mater. Res. **5,** 2277 (1990).

[49] K. N. Tu and A. Howie, Forbidden 200 diffraction spots in silicon, Philos. Mag. B **37,** 73 (1978).

[50] L. Zhu, R. E. Cohen, and T. A. Strobel, Phase transition pathway sampling via swarm intelligence and graph theory, J. Phys. Chem. Lett. **10,** 5019 (2019).

[51] D. Sheppard, P. Xiao, W. Chemelewski, D. D. Johnson, and G. Henkelman, A generalized solid state nudged elastic band method, J. Chem. Phys. **136,** 074103 (2012).